Physics of the Earth and Planetary Interiors, manuscript No.
(will be inserted by the editor)

3D seismic modeling in geothermal reservoirs with a distribution of steam patch sizes, permeabilities and saturations, including ductility of the rock frame

Short title: Seismic wave simulation in geothermal reservoirs

José M. Carcione · Flavio Poletto · Biancamaria Farina · Cinzia Bellezza

Received: date / Accepted: date

Abstract Seismic propagation in the upper part of the crust, where geothermal reservoirs are located, shows generally strong velocity dispersion and attenuation due to varying permeability and saturation conditions and is affected by the brittleness and/or ductility of the rocks, including zones of partial melting. From the elastic-plastic aspect, the seismic properties (seismic velocity, quality factor and density) depend on effective pressure and temperature. We describe the related effects with a Burgers mechanical element for the shear modulus of the dry-rock frame. The Arrhenius equation combined to the octahedral stress criterion define the Burgers viscosity responsible of the brittle-ductile behaviour.

The effects of permeability, partial saturation, varying porosity and mineral composition on the seismic properties is described by a generalization of the White mesoscopic-loss model to the case of a distribution of heterogeneities of those properties. White model involves the wave-induced fluid flow attenuation mechanism, by which seismic waves propagating through small-scale heterogeneities, induce pressure gradients between regions of dissimilar properties, where part of the energy of the fast P-wave is converted to slow P (Biot)-wave. We consider a range of variations of the radius and size of the patches and thin layers whose probability density function is defined by different distributions. The White models used here are that of spherical patches (for partial saturation) and thin layers (for permeability heterogeneities). The complex bulk modulus of the composite medium is obtained with the Voigt-Reuss-Hill average. Effective pressure effects are taken into account by using exponential functions.

We then solve the 3D equation of motion in the space-time domain, by approximating the White complex bulk modulus with that of a set of Zener elements connected in series. The Burgers and generalized Zener models allows us to solve the equations with a direct grid method by the introduction of memory variables. The algorithm uses the Fourier pseudospectral method to compute the spatial derivatives. It is tested against an analytical solution obtained with the correspondence principle. We consider two main cases, namely the same rock frame (uniform porosity and permeability) satu-

Istituto Nazionale di Oceanografia e di Geofisica Sperimentale (OGS), Borgo Grotta Gigante 42c, 34010 Sgonico, Trieste, Italy.
E-mail: jcarcione@inogs.it

rated with water and a distribution of steam patches, and water-saturated background medium with thin layers of dissimilar permeability. Our model indicates how seismic properties change with the geothermal reservoir temperature and pressure, showing that both seismic velocity and attenuation can be used as a diagnostic tool to estimate the in-situ conditions.

Keywords Mesoscopic loss · brittle · ductile · Zener model · Burgers model · seismic-wave simulation · distribution of patch sizes · Fourier method.

1 Introduction

The seismic characterization of porous and fractured crustal rocks, such as anelasticity due to varying permeability and/or saturation and the brittle-ductile behavior, is essential in geothermal exploration, since it plays an important role in determining the availability of geothermal energy. Carcione and Poletto (2013) have introduced an elastic-plastic rheology based on the Burgers mechanical model (e.g., Mainardi and Spada, 2011) to describe the brittle-ductile behaviour on the basis of variations of the shear modulus as a function of temperature. This rheology has been shown to model seismic waves in the crust and mantle, where zones of partial melting occur. The Burgers element allows us to model the effects of the steady-state creep flow on the dry-rock frame. The stiffness components of the brittle and ductile media depend on stress and temperature through the shear viscosity, which is obtained by the Arrhenius equation using the octahedral stress criterion, including the tectonic stress.

The prediction of permeability, the capacity of a material to transmit fluid, is essential in geothermal studies (Manning and Ingebritsen, 1999). Permeability plays an important role in heat and mass transfer and crustal rheology. It is known that permeability can be obtained from seismic data (e.g., Feng and Mannseth, 2010). Therefore, a theory predicting seismic velocity and attenuation including this important property is required. The modeling proposed here also considers the wave-induced attenuation. Wave-induced fluid flow explains the high attenuation of low-frequency waves in fluid-saturated rocks. When seismic waves propagate through small-scale heterogeneities, pressure gradients are induced between regions of dissimilar properties. White (1975), White et al. (1975) and Johnson (2001) have shown that attenuation and velocity dispersion measurements can be explained by the combined effect of mesoscopic-scale inhomogeneities and energy transfer between wave modes, with P-wave to slow P (Biot)-wave conversion being the physical mechanism. We refer to this mechanism as mesoscopic loss (Ba et al., 2015). The mesoscopic-scale length is intended to be larger than the grain sizes but much smaller than the wavelength of the pulse. For instance, if the matrix porosity varies significantly from point to point, diffusion of pore fluid between different regions constitutes a mechanism that can be important at seismic frequencies. A review of the different theories and authors, who have contributed to the understanding of this mechanism, can be found, for instance, in Carcione (2014).

Regarding geothermal reservoirs, the mesoscopic-loss model has been recently applied to seismic modeling by Grab et al. (2017) using the COMSOL Multiphysics$^{\mathrm{R}}$ finite-element solver. Their modeling results show that large attenuation peaks are present for a rock volume containing a network of open fractures (high permeability). The characteristic frequency, at which the attenuation reaches its peak, is linked with the fluid mobility, which is a measure of hydraulic permeability and fluid viscosity. At low seismic frequencies, the attenuation is observed to be controlled by mesoscopic fluid flow while at sonic to ultrasonic frequencies, attenuation is associated with squirt flow. The squirt-flow model has a single free parameter represented by the aspect ratio of the grain contacts. Seismic modeling, including both the Burgers model and the squirt-flow effect, has been performed by Carcione et al. (2017). These authors have generalized a preceding theory based on Gassmann (low-frequency) moduli to the more general case of the presence of local (squirt) flow and global (Biot) flow, which contribute with additional attenuation mechanisms to the wave propagation (Poletto et al., 2017). Grab et al. (2017) conclusively show that indicators for reservoir permeability and fluid content are deducible from the magnitude of seismic attenuation and the critical frequency at which the peak of attenuation and maximum velocity dispersion occur.

In this work, the effects of varying permeability, partial saturation, porosity and mineral composition are described by a generalization of the White mesoscopic-loss model to the case of a distribution of those properties. We consider a range of variations of the radius of the (spherical) patches based on probability density functions. The complex bulk modulus of the composite medium is obtained with the Voigt-Reuss-Hill (VRH) average. This average is based on iso-strain (Voigt) and iso-stress (Reuss) approximations (the stress and strain are unknown and are expected to be non-uniform). The VRH estimates were found in most cases to have an accuracy comparable to that of the self-consistent schemes and are valid for complex rheologies such as general anisotropy (e.g., Man and Huang, 2011). Here, effective pressure effects are taken into account by using exponential functions.

Alternative models describing attenuation and velocity dispersion in heterogeneous media have been developed by Shapiro and Müller (1999), Toms et al. (2006) and Müller et al. (2008), where the authors consider a multiple-scattering approach to approximate the scattered field of a system of randomly distributed poroelastic inclusions. Correlation functions of the spatial heterogeneities, such as the von Kármán function, are used in these works. They show that due to the heterogeneities of poroelastic structures, the attenuation of P-waves is influenced by the permeability in an enhanced way. Moreover, they find that the effects of the patch geometry are not important, even if the attenuation peak for the random model is broader and smaller in amplitude than that of the White periodic model, the frequency dependence of attenuation and velocity are very similar.

Since it is not practical to model explicitly the mesoscopic patches and thin layers in seismic modeling, White effective-medium theory provides a method to implement the related anelastic effects efficiently. This is achieved by approximating the White complex bulk modulus with that of a set of Zener elements connected in series. Then, the Burgers and generalized Zener models allows us to solve the equations with a direct grid method by the introduction of memory variables. Moreover, zones of high permeability, such as a single fracture, can be described with the present full waveform modeling algorithm, by obtaining the stiffness moduli and permeability as a function of porosity, using the Krief and Kozeny-Carman equations, respectively.

We recast the wave equation in the time-domain using the particle-velocity/stress formulation. The model is discretized on a mesh, and the spatial derivatives are calculated with the Fourier method by using the Fast Fourier Transform. The algorithm is verified with an analytical solution obtained by applying the correspondence principle to the frequency-domain elastic analytical solution (e.g., Pilant, 1979, p. 67), and then performing an inverse Fourier transform back to the time domain. We consider two main cases, namely the same rock frame (uniform permeability) saturated with water and a distribution of steam patches, and a water saturated medium with thin layers of dissimilar permeability.

2 Mesoscopic-loss model for a distribution of saturation and permeability

The effects of heterogeneous permeability and fluid saturation are determined from a mesoscopic rock-physics theory (White, 1975; White et al., 1975; Mavko et al, 2009), which provides realistic values of attenuation as a function of porosity, steam saturation, fluid viscosity and permeability (Appendix A). It is assumed that the medium has patches of mesoscopic heterogeneities in a uniform background, where mesoscopic means smaller than the wavelength and larger than the pore size. White's model (see Carcione et al., 2003; Carcione, 2014) describes wave velocity and attenuation as a function of frequency for a given size, a, of the mesoscopic patches.

White (1975) developed the theory for a gas-filled sphere of porous medium of radius a located inside a water-filled cube of porous medium. For simplicity in the calculations, White considered an outer sphere of radius b ($b > a$), instead of a cube, where the gas saturation is $S_g = a^3/b^3$.

Here, we use a generalization of his theory to an heterogeneous frame and a distribution of radii $a_j,\ j = 1, \ldots, J$. The following also holds for a fixed radius and a distribution of saturations S_{1j}. Several probability density (PDF) functions can be used. The normal distribution from $a_0 - \Delta a$ to $a_0 + \Delta a$ is given by the Gaussian function

$$\mathrm{PDF}_j = \frac{\delta}{\sqrt{2\pi}\sigma} \exp[-(a_j - a_0)^2/(2\sigma^2)], \tag{1}$$

where a_0 is the dominant radius and σ is the variance of the distribution. There are J radii equi-spaced at intervals $\delta = 2\Delta a/(J - 1)$. The Rayleigh PDF from 0 to 4 a_0 is

$$\mathrm{PDF}_j = \frac{2\pi a_j}{(J-1)a_0} \exp\left[-\frac{\pi}{4}\left(\frac{a_j}{a_0}\right)^2\right], \tag{2}$$

where a_0 is the mean radius. The uniform PDF from $a_0 - \Delta a$ to $a_0 + \Delta a$ is

$$\mathrm{PDF}_j = \frac{1}{J}. \tag{3}$$

In all the cases it is $\sum_j \mathrm{PDF}_j = 1$. Other distributions can be found in den Engelsen et al. (2002).

According to Appendix A, we obtain J complex moduli K_j describing the anelastic properties of each porous medium with radius a_j. We assume that the composite bulk modulus is given by the Voigt-Reuss-Hill (VRH) average. The Voigt and Reuss averages are iso-strain and iso-stress approximations, respectively (the stress and strain are unknown and are expected to be non-uniform). The VRH estimates were found in most cases to have an accuracy comparable to those obtained by more sophisticated techniques such as self-consistent schemes and are valid for complex rheologies such as general anisotropy and arbitrary grain topologies (e.g., Man and Huang, 2011). Then, based on equation (43), the bulk modulus of the porous medium filled with water and a distribution of steam patches is

$$K = \frac{1}{2}(K_V + K_R), \tag{4}$$

where

$$K_V = \sum_j \mathrm{PDF}_j K_j \quad \text{and} \quad K_R^{-1} = \sum_j \mathrm{PDF}_j K_j^{-1} \tag{5}$$

and the same approach for the shear modulus.

The effective density is given by the arithmetic average

$$\rho = \sum_j \mathrm{PDF}_j \rho_j . \tag{6}$$

For a given patch radius a, the location of the relaxation peak is

$$f_p = \frac{\kappa_2 K_{E2}}{\pi \eta_2 (b-a)^2} = \frac{\kappa_2 K_{E2}}{\pi \eta_2 a^2 (S_g^{1/3} - 1)^2} \tag{7}$$

(White, 1975; Carcione, 2014) (see Appendix A, equation (52)), where the subindex "2" corresponds to the fluid (water). Increasing a implies decreasing the peak frequency. Note that we could represent other properties as PDF, such as viscosity and fluid bulk properties. On the other hand, for permeability heterogeneities, we use White et al. (1975) model (see Appendix A) and instead of a radius, the thickness of the layers are randomly represented with the PDF.

Since the numerical seismic modeling is performed in the time domain, we approximate the VRH complex bulk modulus with that of a set of Zener elements (e.g., Picotti et al, 2010) (see the next Section).

3 The anelastic mechanical model

The constitutive equation, including both the viscoelastic (mesoscopic and shear seismic losses) and brittle-ductile behaviour, can be written as a generalization of the stress-strain relation reported in Carcione and Poletto (2013).

3.1 Seismic anelasticity and brittleness-ductility due to shear deformations

The Burgers model is a series connection of a dashpot and a Zener model as can be seen in Figure 1. The usual expression in the time domain is the creep function

$$\chi = \left(\frac{t}{\eta_B} + \frac{1}{\mu_0} \left[1 - \left(1 - \frac{\tau_\sigma}{\tau_\epsilon} \right) \exp(-t/\tau_\epsilon) \right] \right) H(t) \tag{8}$$

(Carcione et al., 2006; Carcione, 2014), where t is time and $H(t)$ is the Heaviside function. The quantities τ_σ and τ_ϵ are seismic relaxation times for shear deformations, μ_0 is the relaxed shear modulus (see below) and η_B is the (Burgers) flow viscosity describing the ductile behaviour related to shear deformations. The frequency-domain shear modulus μ can be obtained as $\mu = [\mathcal{F}(\dot{\chi})]^{-1}$, where $\mathcal{F}$ denotes time Fourier transform and a dot above a variable denotes time derivative. It gives

$$\mu = \mu_0 \left(\frac{1 + \mathrm{i}\omega\tau_\sigma}{1 + \mathrm{i}\omega\tau_\epsilon} - \frac{\mathrm{i}\mu_0}{\omega \eta_B} \right)^{-1} , \tag{9}$$

where $\mathrm{i} = \sqrt{-1}$ and ω is the angular frequency. The shear relaxation times can be expressed as

$$\tau_\epsilon = \frac{\tau_0}{Q_0}\left(\sqrt{{Q_0}^2+1}+1\right), \quad \tau_\sigma = \tau_\epsilon - \frac{2\tau_0}{Q_0}, \tag{10}$$

where τ_0 is a relaxation time such that $\omega_0 = 1/\tau_0$ is the center frequency of the relaxation peak and Q_0 is the minimum quality factor.

The limit $\eta_B \to \infty$ in equation (9) recovers the Zener kernel to describe the behaviour of the brittle material, while $\tau_\sigma \to 0$ and $\tau_\epsilon \to 0$ yield the Maxwell model used by Dragoni and Pondrelli (1991):

$$\mu = \mu_0 \left(1 - \frac{\mathrm{i}\mu_0}{\omega\eta_B}\right)^{-1} \tag{11}$$

(e.g., Carcione, 2014). For $\eta_B \to 0$, $\mu \to 0$ and the medium becomes a fluid. Moreover, if $\omega \to \infty$, $\mu \to \mu_U = \mu_0\tau_\epsilon/\tau_\sigma$, and μ_0 is the relaxed ($\omega = 0$) shear modulus of the Zener element ($\eta_B = \infty$).

The Burgers viscosity η_B can be expressed by the Arrhenius equation (e.g., Carcione et al., 2006; Montesi, 2007). It is given by

$$\eta_B = \frac{\sigma_o^{1-n}}{2A}\exp(E/RT), \tag{12}$$

where σ_o is the octahedral stress,

$$\sigma_o = \frac{1}{3}\sqrt{(\sigma_v-\sigma_h)^2+(\sigma_v-\sigma_H)^2+(\sigma_h-\sigma_H)^2} \tag{13}$$

(e.g., Carcione and Poletto, 2013), where the σ's are the stress components in the principal system, corresponding to the vertical (v) lithostatic stress, and the maximum (H) and minimum (h) horizontal tectonic stresses, A and n are constants, E is the activation energy, R = 8.3144 J/mol/$^{\mathrm{o}}$K is the gas constant and T is the absolute temperature. The form of the empirical relation (12) is determined by performing experiments at different strain rates, temperatures and/or stresses (e.g., Gangi, 1983; Carter and Hansen, 1983).

3.2 Dilatational anelasticity due to wave-induced fluid flow

We consider a parallel connection of L Zener elements to approximate the composite bulk modulus (4). The dilatational relaxation function is

$$\psi_K(t) = K_0\left[1 - \frac{1}{L}\sum_{l=1}^{L}\left(1-\frac{\tau_{\epsilon l}}{\tau_{\sigma l}}\right)\exp(-t/\tau_{\sigma l})\right]H(t), \tag{14}$$

where $\tau_{\epsilon l}$ and $\tau_{\sigma l}$ are the relaxation times and K_0 is the relaxed bulk modulus. The complex modulus can be expressed as

$$K(\omega) = \frac{K_0}{L}\sum_l\left(\frac{1+\mathrm{i}\omega\tau_{\epsilon l}}{1+\mathrm{i}\omega\tau_{\sigma l}}\right). \tag{15}$$

In order to include in the equation of motion pressure effects, we express the bulk moduli as

$$K \to K g_1(p_e), \quad \text{and} \quad \mu \to \mu g_2(p_e), \tag{16}$$

where $g_r(p_e),\ r = 1, 2$ defines the dependence of the moduli on the effective pressure $p_e = p_c - np$, where p_c is the confining pressure, p is the pore (fluid) pressure, n is the effective stress coefficient, and K_0 and μ_0 are the bulk and shear moduli at infinite effective pressure and $\eta_B = \infty$ (or $\omega = \infty$).

Laboratory experiments show that under hydrostatic pore pressure, confining stress and differential pressure dependences of elastic moduli are phenomenologically described by the following relationship

$$g_r(p_e) = a_r + b_r p_e - c_r \exp(-p_e/p_r^*), \quad r = 1, 2 \tag{17}$$

(Kaselow and Shapiro, 2004; Carcione, 2014), where a_r, b_r, c_r and p_r^* are fitting parameters for a given set of measurements. If $n_r = 1$, $p_e = p_d = p_c - p$, the differential pressure. The simplest form of function g, in good agreement with experimental data, is obtained for $a_r = 1$, $b_r = 0$, $c_r = 1 - d_r$ and $n_r = 1$, i. e.,

$$g_r(p_d) = 1 - (1 - d_r) \exp(-p_d/p_r^*), \quad r = 1, 2, \tag{18}$$

where g_r =1 for $p_d \to \infty$ (e.g., very high confining pressure) and $g_r = d_r$ for $p_d \to 0$ (pore pressure equal to the confining pressure).

4 Equations of motion

In order to obtain the equations of motion to describe wave propagation it is convenient to consider the Burgers relaxation function

$$\psi_\mu(t) = [A_1 \exp(-t/\tau_1) - A_2 \exp(-t/\tau_2)]H(t) \tag{19}$$

(Carcione, 2014; Carcione and Poletto, 2013), where

$$\tau_{1,2} = -\frac{1}{\omega_{1,2}} \quad \text{and} \quad A_{1,2} = \frac{\mu_1\mu_2 + \omega_{1,2}\eta_\epsilon\mu_2}{\eta_\epsilon(\omega_1 - \omega_2)}. \tag{20}$$

and

$$(2\eta_B\eta_\epsilon)\omega_{1,2} = -b \pm \sqrt{b^2 - 4\mu_1\mu_2\eta_B\eta_\epsilon}, \qquad b = (\mu_1 + \mu_2)\eta_B + \mu_2\eta_\epsilon. \tag{21}$$

In terms of the relaxation times and μ_0, it is

$$\mu_1 = \frac{\mu_0\tau_\epsilon}{\tau_\epsilon - \tau_\sigma}, \quad \mu_2 = \mu_0\frac{\tau_\epsilon}{\tau_\sigma}, \quad \eta_\epsilon = \mu_1\tau_\epsilon. \tag{22}$$

The complex shear modulus is

$$\mu = \mathcal{F}(\dot{\psi}_\mu) = \mathrm{i}\omega\left(\frac{A_1\tau_1}{1 + \mathrm{i}\omega\tau_1} - \frac{A_2\tau_2}{1 + \mathrm{i}\omega\tau_2}\right). \tag{23}$$

It can be verified that equations (9) and (23) coincide.

The stress-strain relation is given by

$$\dot{\sigma}_{ij} = \dot{\psi}_K * \vartheta\delta_{ij} + 2\dot{\psi}_\mu * \left(\dot{\epsilon}_{ij} - \frac{1}{3}\dot{\epsilon}_{kk}\delta_{ij}\right), \tag{24}$$

where σ are stress components, ϵ are strain components, $\vartheta = \dot{\epsilon}_{ii} = \partial_i v_i$ is the dilatation field, v are particle-velocity components, ∂_i indicates a spatial derivative with respect to the variable x_i, i = 1,2,3 ($x_1 = x$, $x_2 = y$ and $x_3 =$ z), δ is Kronecker delta and "$*$" denotes time convolution.

The velocity-stress formulation is

$$\dot{\sigma}_{ij} = \dot{\psi}_K * \partial_k v_k \delta_{ij} + \dot{\psi}_\mu * \left(\partial_i v_j + \partial_j v_i - \frac{2}{3} \partial_k v_k \delta_{ij} \right), \tag{25}$$

where we have used the velocity-rate of strain relation $\dot{\epsilon}_{ij} = \frac{1}{2}(\partial_i v_j + \partial_j v_i)$.

All the convolutions have the form $\dot{\psi} * \partial_i v_j$ and can be avoided by introducing memory variables. We obtain,

$$\dot{\psi}_K * \vartheta = K_U \left(\vartheta + \sum_l e_l \right) = K_U \left(\partial_k v_k + \sum_l e_l \right), \tag{26}$$

where

$$K_U = \frac{K_0}{\beta L}, \quad \beta = \left(\sum_l \frac{\tau_{\epsilon l}}{\tau_{\sigma l}} \right)^{-1} \tag{27}$$

is the unrelaxed modulus, and e_l are dilatational memory variables,

$$e_l = \varphi_l H * \vartheta, \quad \varphi_l = \frac{\beta}{\tau_{\sigma l}} \left(1 - \frac{\tau_{\epsilon l}}{\tau_{\sigma l}} \right) \exp(-t/\tau_{\sigma l}), \tag{28}$$

satisfying

$$\dot{e}_l = \frac{1}{\tau_{\sigma l}} \left[\beta \left(1 - \frac{\tau_{\epsilon l}}{\tau_{\sigma l}} \right) \vartheta - e_l \right] \tag{29}$$

(Carcione, 2014).

On the other hand,

$$\dot{\psi}_\mu * \partial_i v_j = A_1 (\partial_i v_j + e_{ij}^{(1)}) - A_2 (\partial_i v_j + e_{ij}^{(2)}), \quad i, j = 1, 3, \tag{30}$$

where

$$e_{ij}^{(l)} = \varphi_l H * \partial_i v_j, \quad \varphi_l = -\frac{1}{\tau_l} \exp(-t/\tau_l), \quad l = 1, 2, \tag{31}$$

which satisfy

$$\dot{e}_{ij}^{(l)} = -\frac{1}{\tau_l} (\partial_i v_j + e_{ij}^{(l)}). \tag{32}$$

The explicit expression of the stress-strain relation (25) is

$$\begin{aligned}
\dot{\sigma}_{xx} &= \dot{\psi}_K * (\partial_x v_x + \partial_y v_y + \partial_z v_z) + \frac{2}{3} \dot{\psi}_\mu * (2\partial_x v_x - \partial_y v_y - \partial_z v_z), \\
\dot{\sigma}_{yy} &= \dot{\psi}_K * (\partial_x v_x + \partial_y v_y + \partial_z v_z) + \frac{2}{3} \dot{\psi}_\mu * (2\partial_y v_y - \partial_x v_x - \partial_z v_z), \\
\dot{\sigma}_{zz} &= \dot{\psi}_K * (\partial_x v_x + \partial_y v_y + \partial_z v_z) + \frac{2}{3} \dot{\psi}_\mu * (2\partial_z v_z - \partial_y v_y - \partial_x v_x), \\
\dot{\sigma}_{xy} &= \dot{\psi}_\mu * (\partial_x v_y + \partial_y v_x), \\
\dot{\sigma}_{xz} &= \dot{\psi}_\mu * (\partial_x v_z + \partial_z v_x), \\
\dot{\sigma}_{yz} &= \dot{\psi}_\mu * (\partial_y v_z + \partial_z v_y).
\end{aligned} \tag{33}$$

Substituting the memory variables according to equations (26) and (30), we obtain

$$
\begin{aligned}
3\dot{\sigma}_{xx} &= 3K_U(\partial_x v_x + \partial_y v_y + \partial_z v_z + \textstyle\sum_l e_l) + 2\left[(A_1 - A_2)(2\partial_x v_x - \partial_y v_y - \partial_z v_z) + \right.\\
&\qquad \left. A_1(2e_{xx}^{(1)} - e_{yy}^{(1)} - e_{zz}^{(1)}) - A_2(2e_{xx}^{(2)} - e_{yy}^{(2)} - e_{zz}^{(2)})\right],\\
3\dot{\sigma}_{yy} &= 3K_U(\partial_x v_x + \partial_y v_y + \partial_z v_z + \textstyle\sum_l e_l) + 2\left[(A_1 - A_2)(2\partial_y v_y - \partial_x v_x - \partial_z v_z) + \right.\\
&\qquad \left. A_1(2e_{yy}^{(1)} - e_{xx}^{(1)} - e_{zz}^{(1)}) - A_2(2e_{yy}^{(2)} - e_{xx}^{(2)} - e_{zz}^{(2)})\right],\\
3\dot{\sigma}_{zz} &= 3K_U(\partial_x v_x + \partial_y v_y + \partial_z v_z + \textstyle\sum_l e_l) + 2\left[(A_1 - A_2)(2\partial_z v_z - \partial_x v_x - \partial_y v_y) + \right.\\
&\qquad \left. A_1(2e_{zz}^{(1)} - e_{xx}^{(1)} - e_{yy}^{(1)}) - A_2(2e_{zz}^{(2)} - e_{xx}^{(2)} - e_{yy}^{(2)})\right].\\
\dot{\sigma}_{xy} &= (A_1 - A_2)(\partial_x v_y + \partial_y v_x) + A_1(e_{xy}^{(1)} + e_{yx}^{(1)}) - A_2(e_{xy}^{(2)} + e_{yx}^{(2)}),\\
\dot{\sigma}_{xz} &= (A_1 - A_2)(\partial_x v_z + \partial_z v_x) + A_1(e_{xz}^{(1)} + e_{zx}^{(1)}) - A_2(e_{xz}^{(2)} + e_{zx}^{(2)}),\\
\dot{\sigma}_{yz} &= (A_1 - A_2)(\partial_y v_z + \partial_z v_y) + A_1(e_{yz}^{(1)} + e_{zy}^{(1)}) - A_2(e_{yz}^{(2)} + e_{zy}^{(2)}).
\end{aligned}
\tag{34}
$$

On the other hand, the dynamical equations of motion are

$$
\begin{aligned}
\dot{v}_x &= \frac{1}{\rho}(\partial_x \sigma_{xx} + \partial_y \sigma_{xy} + \partial_z \sigma_{xz}) + s_x,\\
\dot{v}_y &= \frac{1}{\rho}(\partial_x \sigma_{xy} + \partial_y \sigma_{yy} + \partial_z \sigma_{yz}) + s_y,\\
\dot{v}_z &= \frac{1}{\rho}(\partial_x \sigma_{xz} + \partial_y \sigma_{yz} + \partial_z \sigma_{zz}) + s_z
\end{aligned}
\tag{35}
$$

(e.g., Carcione, 2014), where s_i are source components.

The equations of motion are given by equations (29), (32), (34) and (35) in the unknown vector $\mathbf{v} = (v_x, v_y, v_z, \sigma_{xx}, \sigma_{yy}, \sigma_{zz}, \sigma_{xy}, \sigma_{xz}, \sigma_{yz}, e_l, e_{ij}^{(l)})^\top$. In matrix notation

$$
\dot{\mathbf{v}} = \mathbf{M} \cdot \mathbf{v} + \mathbf{s}, \tag{36}
$$

where $\mathbf{M}$ is a $27{+}L \times 27{+}L$ matrix containing the material properties and spatial derivatives.

4.1 Wave velocities and attenuation

The wave velocities can be obtained from the density and equation (24), which represents the stress-strain relations of an isotropic-viscoelastic medium. We make use of the frequency-domain version of the stress-strain relations and $\mu = \left[\mathcal{F}(\dot{\psi}_\mu)\right]$. Note that $\dot{\psi}_\mu * \dot{\chi} = \delta$, where δ is Dirac's function (e.g., Carcione, 2014). Then, the complex and frequency-dependent P- and S-wave velocities are

$$
v_P(\omega) = \sqrt{\frac{K + 4\mu/3}{\rho}}, \quad \text{and} \quad v_S(\omega) = \sqrt{\frac{\mu}{\rho}}, \tag{37}
$$

respectively, where the density is given by equation (6).

For homogeneous waves in isotropic media, the phase velocity and attenuation factors are given by

$$c = \left[\mathrm{Re}\left(\frac{1}{v}\right)\right]^{-1} \tag{38}$$

and

$$\alpha = -\omega \mathrm{Im}\left(\frac{1}{v}\right), \tag{39}$$

and the P- and S-wave quality factors are given by

$$Q = \frac{\mathrm{Re}(v^2)}{\mathrm{Im}(v^2)} \tag{40}$$

(e.g., Carcione 2014), where v represents either v_P or v_S.

The complex bulk modulus $K(\omega)$ (15) is obtained by fitting the generalized White complex modulus (4).

5 Examples

For geothermal studies, the water properties as a function of pressure and temperature can be obtained from the fluid thermo-physical database provided in the website of the National Institute of Standards and Technology (NIST), collected from laboratory measurements by Lemmon et al. (2005). In "Thermophysical Properties of Fluid Systems", we choose water (1) and isothermal Properties (3). The range of allowable values are [0, 1000] $^{\mathrm{o}}$C and [0, 1000] MPa. Figure 1 shows typical values of the acoustic properties. The bulk modulus is given by $K_f = \rho_w c_w^2$, where ρ_w and c_w are the water density and sound velocity.

Table 1 shows the properties of the fluid patches and permeability heterogeneities that affect the background values (lower table). First, we consider the properties for partial saturation (upper table) to illustrate how to approximate the White modulus with Zener elements. Figure 2 shows the normal and Rayleigh distributions and Figure 3 displays the phase velocity and dissipation factor obtained with different PDF: "1 radius" correspond to a value a = 0.5 cm, "3 radii" corresponds to a uniform distribution of a = 0.1, 0.5 and 0.9 cm, and "J radii" is the uniform distribution with J = 100 radii. The results of the Rayleigh and uniform PDF are similar. Let us obtain the generalized Zener parameters to represent the 3-radii bulk modulus. The high-frequency limit modulus is $K_U = K_\infty$ (see equations (15), (27) and (45)). Figure 4 shows the fit to K (equation (4)) (dots), where (a) is the associated phase velocity and (b) is the dissipation factor, Re(K)/Im(K). We have used three Zener elements with parameters f_{01} = 0.44 Hz, f_{02} = 1.43 Hz, f_{03} = 35.7 Hz, Q_{01} = 13, Q_{02} = 6, Q_{03} = 5.9 and K_0 = 3.14 GPa, according to the parameterization (10), where $f_0 = 1/(2\pi\tau_0)$. Since the Zener peaks resemble the White peaks we have not attempted a fit using a minimization algorithm, which could further improve the match.

Now, let us consider a constant a radius and describe the gas saturation S_1 (S_g) with a normal PDF distribution. In this case $a = S_1/b^{1/3}$ (see first paragraph in Appendix A.1). We assume a mean value S_{10} = 0.4 (it plays the role of a_0 in equation (2)), a variance σ = 0.1 and ΔS_1 = 0.4. Figure 5 shows the normal PDF (a) and the phase velocity (b) and dissipation factor associated to the White bulk modulus. The

Zener approximation uses two elements with $f_{01} = 13$ Hz, $f_{02} = 3.8$ Hz, $Q_{01} = 7.8$, $Q_{02} = 9$ and $K_0 = 8.5$ GPa.

Next, we analyze the effects of permeability using equation (50) and the properties of Table 1. The period of the stratification is $L = 1$ m. The grain properties of phases 1 (heterogeneities) and 2 (background) are the same, i.e, those of the background medium. On the basis of a normal distribution of the proportion p_1 ($p_{10} = 0.5$, $\Delta p_1 = 0.4$, $\sigma = 0.1$ and $J = 100$), Figure 6 shows the phase velocity and quality factor and the Zener approximation with two elements ($f_{01} = 9.9$ Hz, $f_{02} = 3.9$ Hz, $Q_{01} = 16$, $Q_{02} = 16$ and $K_0 = 9.66$ GPa.) Now, we vary the permeability of the heterogeneities using a uniform distribution and keep the size constant and equal to 0.5 m. The permeability varies uniformly from 10^{-9} m^2 to 10^{-15} m^2, i.e. from 1000 to 10^{-3} darcy ($J = 100$). Figure 7 shows the phase velocity (a) and dissipation factor (b) associated with the White P-wave modulus. The red line corresponds to $\kappa_1 = 1$ darcy.

The concept of fluid mobility (permeability divided by the fluid viscosity),

$$M = \frac{\kappa}{\eta_f},$$

is widely used to define the frequency dependence of seismic velocity and attenuation (e.g., Batzle et al., 2006). High fluid mobility permits pore-pressure equilibrium between heterogeneous regions, resulting in a low-frequency state where Gassmann equation is valid. On the contrary, low fluid mobility implies strong dispersion, even within the seismic band. Here, the low-frequency assumption fails. The velocity dispersion and attenuation (mesoscopic loss) is due to the presence of the Biot slow wave. Consider the case of fine layers (equation (50)). The diffusivity constant is $d = \kappa K_E/\eta_f$. The critical fluid-diffusion relaxation length is $L = \sqrt{d/\omega}$. The fluid pressures will be equilibrated if L is comparable to the period of the stratification. For smaller diffusion lengths (e.g., higher frequencies) the pressures will not be equilibrated, causing strong attenuation and velocity dispersion. Notice that the reference frequency (52) is obtained for a diffusion length $L = l_1/4$. Actually, the key quantity defining the relaxation peaks is fluid mobility. It can easily be seen that permeability and viscosity are involved as a ratio in the equations of Appendices A.1 and A.2. However changes in permeability are more significant since its range is wider than that of viscosity (orders of magnitudes from sandstones to shales).

In the following, we illustrate how the seismic velocity varies with saturation and permeability (the frequency is 10 Hz). Figure 8 displays the P-wave phase velocity (38) (a) and dissipation factor (40) (b) as a function of steam saturation predicted by the generalized White model based on the Rayleigh PDF ($a_0 = 0.5$ m, $J = 100$). Velocity clearly decreases with increasing steam saturation while the dissipation factor has a maximum at approximately 30 % saturation. Figure 9 shows the phase velocity (a) and dissipation factor (b) as a function of the background permeability. The permeability heterogeneities follow a uniform PDF and the size is 0.5 m. There is a relaxation peak similar to the frequency peaks. The maximum occurs at $\kappa_2 = 10^{-12.74}$ m^2 $= 0.18$ darcy (the operation 10^{12-p} converts to darcy). A plot as a function of fluid mobility ($M_2 = \kappa_2/\eta_2$) is identical, but with the abscissa values scaled by $1/\eta_2$.

First, we test the numerical code against the 3D analytical solution for P-S waves in homogeneous media (Appendix B). To compute the transient responses, we use a Ricker wavelet of the form:

$$w(t) = \left(a - \frac{1}{2}\right)\exp(-a), \quad a = \left[\frac{\pi(t - t_s)}{t_p}\right]^2, \tag{41}$$

where t_p is the period of the wave (the distance between the side peaks is $\sqrt{6}t_p/\pi$) and we take $t_s = 1.4t_p$. Its frequency spectrum is

$$W(\omega) = \left(\frac{t_p}{\sqrt{\pi}}\right) \bar{a} \exp(-\bar{a} - \mathrm{i}\omega t_s), \quad \bar{a} = \left(\frac{\omega}{\omega_p}\right)^2, \quad \omega_p = \frac{2\pi}{t_p}. \tag{42}$$

The peak frequency is $f_p = 1/t_p$.

We consider the case given in Figure 5, and two values of the Burgers viscosity, namely $\eta_B = 10^{20}$ Pa s and $\eta_B = 2 \times 10^8$ Pa s. In the second case, the S wave is highly attenuated due to melting (extreme ductility). The shear seismic quality factor is assumed to be infinite. The numerical mesh (a cube) has 81^3 grid points and a grid spacing of $dx = dy = dz = 20$ m. The source is a vertical force ($s_x = s_y = 0$ and $s_z = w(t)$), with $f_p = 15$ Hz and the receiver is located at $x = 200$ m, $y = 0$ m and $z = 300$ m from the source. The solution is computed using a time step $dt = 2$ ms. Figure 10 shows the comparison between the numerical and analytical solutions for the two values of η_B, where (a) and (c) correspond to v_1 and (b) and (d) to v_3. The agreement is excellent is all the cases.

In order to illustrate the effect of attenuation, Figure 11 shows the comparison between the solutions without and with the mesoscopic loss for $\eta_B = 10^{20}$ Pa s. We show the P wave since the S wave is not affected. As can be seen, there is attenuation and strong velocity dispersion due to the effects caused by the saturation distribution (Figure 5a). The lossless wavefield is slower than the lossy wavefield due to the fact that the lossless case has been chosen in the low-frequency limit ($K \to K_0$ in equation (15). What is relevant is that different frequency windows travel with a different phase velocity (Figure 5b).

The modeling algorithm allows us to compute snapshots of the wavefield, which are useful for the interpretation of the seismograms. Snapshots at the (x, z)-plane are shown in Figure 12, where (a) and (b) correspond to the v_x-component for $\eta_B = 10^{20}$ Pa s, with (a) and without (b) mesoscopic-loss. As in the seismograms shown in Figure 11, there is a strong attenuation of the P wave and the S wave (inner wavefront) is not affected.

6 Conclusions

Geothermal reservoirs behave brittle and ductile depending on the in-situ temperature and pressure conditions and show strong mesoscopic-type anelasticity due to zones of high permeability (high porosity) and partial fluid saturation. These factors affect seismic waves (phase velocity and attenuation) to the extent that the seismic properties can be good indicators for ductility (partial melting), reservoir permeability and fluid content. The critical frequency at which the peak of attenuation and maximum velocity dispersion occur is an additional indicator.

We present a methodology to model the seismic properties of geothermal reservoirs, including ductility, by using a poro-viscoelastic description, based on White mesoscopic-loss theory and the Burgers mechanical model. Losses due to dilatational deformations are described by a generalization of the White model to the case of a distribution of heterogeneities based on different distribution functions. The rheological equation is implemented in seismic numerical modeling by means of a generalized Zener model and memory variables, where the governing equations are solve with a pseudospectral method. The Burgers model describes seismic attenuation due to shear deformations. Moreover, the theory can model variations of the properties due to changes in temperature and confining and pore pressure. The wet-rock seismic velocities can explicitly be obtained as a function of the water properties at critical and supercritical conditions. We show how a distribution of saturation and permeability heterogeneities affect the amplitude and attenuation of the wavefield. The numerical solution is tested against and analytical solution obtained with the correspondence principle. The agreement between solution is excellent. Future research will consider the presence of anisotropy due to oriented fractures.

Acknowledgments: This work was partially supported by the MATER (WP4 MATER-GEO) project.

References

Ba, J., Carcione, J. M., Du, O., Zhao, H., and Müller, T. M., 2015, Seismic exploration of hydrocarbons in heterogeneous reservoirs, New theories, methods and applications, Elsevier Science.

Batzle, M. L., Han, D.-H., and Hofmann, R., 2006, Fluid mobility and frequency-dependent seismic velocity – Direct measurements, Geophysics, 71, N1-N9.

Carcione, J. M., 2014, Wave fields in real media: Wave propagation in anisotropic, anelastic, porous and electromagnetic media. Handbook of Geophysical Exploration, vol. 38, Elsevier (3nd edition, revised and extended).

Carcione, J. M., Helle, H. B., and Pham, N. H., 2003. White's model for wave propagation in partially saturated rocks: Comparison with poroelastic numerical experiments, Geophysics, 68, 1389–1398.

Carcione, J. M., Helle, H. B., and Gangi, A. F., 2006, Theory of borehole stability when drilling through salt formations, Geophysics, 71, F31–F47.

Carcione, J. M., and Poletto, F., 2013, Seismic rheological model and reflection coefficients of the brittle-ductile transition, Pure and Applied Geophysics, 170, 2021–2035.

Carcione, J. M., and Poletto, F., and Farina, B., 2017, The Burgers/squirt-flow seismic model of the crust and mantle, Physics of the Earth and Planetary Interiors, accepted.

Carter, N. L., and Hansen, F. D., 1983 Creep of rocksalt, Tectonophysics, 92, 275–333.

Man, C.-S., and Huang, M., 2011, A simple explicit formula for the Voigt-Reuss-Hill average of elastic polycrystals with arbitrary crystal and texture symmetries, J. Elast., 105, 29–48.

den Engelsen, C. W., Isarin, J. C., Gooijer, H., Warmoeskerken, M. M. C. G., and Groot Wassink, J., 2002, Bubble size distribution of foam, AUTEX Research J., 2.

Dragoni, M., and Pondrelli, S., 1991, Depth of the brittle-ductile transition in a transcurrent boundary zone, Pure and Applied Geophysics, 135, 447–461.

Feng, T., and Mannseth, T., 2010, Impact of time-lapse seismic data for permeability estimation, Comput. Geosci., 14, 705–719.

Gangi, A.F., 1983, Transient and steady-state deformation of synthetic rocksalt, Tectonophysics, 91, 137–156.

Grab, M., Quintal, B., Caspari, E., Maurer, H., and Greenhalgh, S., 2017, Numerical modeling of fluid effects on seismic properties of fractured magmatic geothermal reservoirs, Solid Earth, 8, 255–279.

Johnson, D.L., 2001, Theory of frequency dependent acoustics in patchy-saturated porous media, Journal of the Acoustical Society of America, 110, 682–694.

Kaselow, A., and Shapiro, S. A., 2004, Stress sensitivity of elastic moduli and electrical resistivity in porous rocks, J. Geophys. Eng., 1, 1–11.

Lemmon, E. W., McLinden, M. O., Friend, D. G., 2005, Thermophysical properties of fluid systems. In: Lindstrom, P.J., Mallard, W.G. (eds.), NIST Chemistry Webbook 69, NIST Standard Reference Database, Gaithersburg, MD, USA, http://webbook.nist.gov/chemistry/.

Mainardi, F., and Spada, G., 2011, Creep, relaxation and viscosity properties for basic fractional models in rheology, The European Physical Journal, Special Topics, 193, 133–160.

Manning, C.E., and Ingebritsen, S. E., 1999, Permeability of the continental crust: the implications of geothermal data and metamorphic systems, Reviews of Geophysics, 37, 127–50.

Mavko, G., Mukerji, T., and Dvorkin, J., 2009. The rock physics handbook: tools for seismic analysis in porous media, Cambridge Univ. Press.

Meissner, R., and Strehlau, J., 1982, Limits of stresses in continental crusts and their relation to the depth-frequency distribution of shallow earthquakes, Tectonics, 1, 73–89.

Müller, T. M., Toms-Stewart, J., Wenzlau, F., 2008, Velocity-saturation relation for partially saturated rocks with fractal pore fluid distribution, 35, L09306, doi:10.1029/2007GL033074, 2008

Picotti, S., Carcione, J. M., Rubino, G., Santos, J. E., and Cavallini, F., 2010, A viscoelastic representation of wave attenuation in porous media, Computer & Geosciences, 36, 44–53.

Pilant, W. L., 1979, Elastic waves in the earth. North-Holland Amsterdam.

Poletto, F., Farina, B., and Carcione, J. M., 2017, Sensitivity of seismic properties to temperature variations in a geothermal reservoir, submitted to Geothermics.

Shapiro, S. A., and Müller T., 1999, Seismic signatures of permeability in heterogeneous porous media, Geophysics, 64, 99–103.

Toms, J., Müller, T. M., and Gurevich, B, 2007, Seismic attenuation in porous rocks with random patchy saturation, Geophys. Prospect., 55(5), 671–678.

White, J. E., 1975. Computed seismic speeds and attenuation in rocks with partial gas saturation, Geophysics 40, 224–232.

White, J. E., Mikhaylova, N. G., and Lyakhovitskiy, F. M., 1975, Low-frequency seismic waves in fluid saturated layered rocks, Izvestija Academy of Sciences USSR, Phys. Solid Earth, 11, 654–659.

A White's model for mesoscopic loss

A.1 Gas patches. Partial saturation

White (1975) has assumed spherical gas pockets much larger than the grains but much smaller than the wavelength. He developed the theory for a gas-filled sphere of porous medium of radius a located inside a water-filled cube of porous medium. For simplicity in the calculations, White considers an outer sphere of radius b ($b > a$), instead of a cube. Thus, the system consists of two concentric spheres, where the volume of the outer sphere is the same as the volume of the original cube. In 3-D space, the outer radius is $b = l/(4\pi/3)^{1/3}$, where l is the size of the cube. In 2-D space, the outer radius is $b = l/\sqrt{\pi}$, where l is the size of the square. The distance between pockets is l. Let us denote the saturation of gas and water by $S_1(S_g)$ and $S_2(S_w)$, respectively, such that $S_1+S_2 = 1$. Then $S_1 = a^3/b^3$ in 3-D space and $S_1 = a^2/b^2$ in 2-D space. When $a = l/2$ the gas pockets touch each other. This happens when $S_1 = \pi/6 = 0.52$ in 3-D space. Therefore, for values of the gas saturation higher than these critical value, or values of the water saturation between 0 and 0.48, the theory is not rigorously valid. Another limitation to consider is that the size of gas pockets should be much smaller than the wavelength, i.e., $a \ll c_r/f$, where c_r is a reference velocity and f is the frequency.

White's equations are given in Mavko et al (2009) and reported in the following for completeness. Assuming that the dry-rock and grain moduli and permeability, κ, of the different regions are the same, the complex bulk modulus as a function of frequency is given by

$$K[\text{single patch size}] = \frac{K_\infty}{1 - K_\infty W}, \tag{43}$$

where

$$\begin{aligned}
W &= \frac{3a^2(R_1 - R_2)(Q_2 - Q_1)}{b^3 \mathrm{i}\omega(Z_1 + Z_2)},\\
\alpha R_1 &= \frac{(K_1 - K_m)(3K_2 + 4\mu_m)}{K_2(3K_1 + 4\mu_m) + 4\mu_m(K_1 - K_2)S_1},\\
\alpha R_2 &= \frac{(K_2 - K_m)(3K_1 + 4\mu_m)}{K_2(3K_1 + 4\mu_m) + 4\mu_m(K_1 - K_2)S_1},\\
(\kappa/\eta_1 a)Z_1 &= \frac{1 - \exp(-2\gamma_1 a)}{(\gamma_1 a - 1) + (\gamma_1 a + 1)\exp(-2\gamma_1 a)},\\
-(\kappa/\eta_2 a)Z_2 &= \frac{(\gamma_2 b + 1) + (\gamma_2 b - 1)\exp[2\gamma_2(b - a)]}{(\gamma_2 b + 1)(\gamma_2 a - 1) - (\gamma_2 b - 1)(\gamma_2 a + 1)\exp[2\gamma_2(b - a)]},\\
\gamma_n &= \sqrt{\mathrm{i}\omega\eta_n/(\kappa K_{En})},\\
K_{En} &= \left[1 - \frac{\alpha K_{fn}(1 - K_n/K_s)}{\phi K_n(1 - K_{fn}/K_s)}\right] M_n,\\
M_n &= \left[\frac{\phi}{K_{fn}} + \frac{1}{K_s}(\alpha - \phi)\right]^{-1},\\
\alpha &= 1 - \frac{K_m}{K_s},\\
Q_n &= \frac{\alpha M_n}{K_n};
\end{aligned} \tag{44}$$

$$K_\infty = \frac{K_2(3K_1 + 4\mu_m) + 4\mu_m(K_1 - K_2)S_1}{(3K_1 + 4\mu_m) - 3(K_1 - K_2)S_1} \tag{45}$$

is the – high frequency – bulk modulus when there is no fluid flow between the gas pockets. K_1 and K_2 are the – low frequency – Gassmann moduli, which are given by

$$K_n = \frac{K_s - K_m + \phi K_m \left(K_s/K_{fn} - 1\right)}{1 - \phi - K_m/K_s + \phi K_s/K_{fn}}, \quad n = 1, 2. \tag{46}$$

At the low-frequency limit, we have the Reuss average of the fluid moduli and the value is

$$K_0 \approx \frac{K_2(K_1 - K_m) + S_1 K_m (K_2 - K_1)}{(K_1 - K_m) + S_1(K_2 - K_1)}, \tag{47}$$

according to Mavko et al. (2009).

The peak relaxation frequency is approximately given by

$$f_p = \frac{\kappa K_{E2}}{\pi \eta_2 (b-a)^2}. \tag{48}$$

The density is obtained as an arithmetic average:

$$\rho = (1-\phi)\rho_s + \phi[(\rho_{f1} - \rho_{f2})S_1 + \rho_{f2}]. \tag{49}$$

A.2 Heterogeneous permeability

In this case, we consider a model that assumes different frame properties of the two frames and the same fluid. The model is given by a stack of two thin alternating porous layers of thickness l_1 and l_2, such that the period of the stratification is $L = l_1 + l_2$ and the proportion if medium 1 and medium 2 are $p_1 = l_1/L$ (the permeability heterogeneities) and $p_2 = l_2/L$ (the background medium in Table 1). Omitting the subindex j for clarity, the complex and frequency dependent P-wave stiffness is given by

$$E = \left[\frac{1}{E_G} + \frac{2(r_2 - r_1)^2}{\mathrm{i}\omega(l_1 + l_2)(I_1 + I_2)}\right]^{-1}, \tag{50}$$

where

$$r = \frac{\alpha M}{E_G}, \quad I = \frac{\eta}{\kappa s}\coth\left(\frac{aL}{2}\right), \quad s = \sqrt{\frac{\mathrm{i}\omega\eta E_G}{\kappa M E_m}}, \tag{51}$$

for each single layer (White et al., 1975; Carcione and Picotti 2006) [see also Carcione (2014), eq. (7.453)], where $E_G = (p_1/E_{G1} + p_2/E_{G2})^{-1}$, $E_{Gj} = K_j + (4/3)\mu_{mj}$ and $E_{mj} = K_{mj} + (4/3)\mu_{mj}$, with j =1 and 2 being the heterogeneities and background media, respectively.

The peak relaxation frequency is approximately given by

$$f_p = \frac{8\kappa_2 K_{E2}}{\pi \eta_2 l_2^2}. \tag{52}$$

The composite shear modulus is given by the Voigt-Reuss-Hill average, i.e,

$$\mu_U = \frac{1}{2}(\mu_R + \mu_V), \quad \mu_R^{-1} = p_1\mu_{m1}^{-1} + p_2\mu_{m2}^{-1}, \quad \text{and} \quad \mu_V = p_1\mu_{m1} + p_2\mu_{m2}, \tag{53}$$

where the subscript "U" means unrelaxed (high frequency limit).

The density is obtained as

$$\rho = [(1-\phi_1)\rho_s + \phi_1\rho_f]p_1 + [(1-\phi_2)\rho_s + \phi_2\rho_f](1-p_1), \tag{54}$$

where we have assumed that the medium has the same mineral.

B Analytical solution

The 3D viscoelastic Green's function can be obtained by generalising the elastic solution using the correspondence principle (e.g., Carcione, 2014). The elastic solution for a vertical force is given in Pilant (1979, p. 69). Here the sign of ω is reversed, since we use the opposite Fourier convention. The displacement Green function in spherical coordinates corresponding to the wave field generated by an impulsive vertical force of strength F_0 is given by

$$
\begin{aligned}
G_r(r,\omega,v_P,v_S,\rho) = \frac{F_0\cos\theta}{4\pi\rho}\Bigg[\frac{1}{r}\exp\left(-\frac{\mathrm{i}\omega r}{v_P}\right)\left(\frac{1}{v_P^2}-\frac{2\mathrm{i}}{\omega r v_P}-\frac{2}{\omega^2 r^2}\right) \\
+\frac{2}{\omega r^2}\exp\left(-\frac{\mathrm{i}\omega r}{v_S}\right)\left(\frac{\mathrm{i}}{v_S}+\frac{1}{\omega r}\right)\Bigg]
\end{aligned}
\tag{55}
$$

$$
\begin{aligned}
G_\theta(r,\omega,v_P,v_S,\rho) = \frac{F_0\sin\theta}{4\pi\rho}\Bigg[-\frac{1}{\omega r^2}\exp\left(-\frac{\mathrm{i}\omega r}{v_P}\right)\left(\frac{\mathrm{i}}{v_P}+\frac{1}{\omega r}\right) \\
-\frac{1}{r}\exp\left(-\frac{\mathrm{i}\omega r}{v_S}\right)\left(\frac{1}{v_S^2}-\frac{\mathrm{i}}{\omega r v_S}-\frac{1}{\omega^2 r^2}\right)\Bigg]
\end{aligned}
\tag{56}
$$

where $r=\sqrt{x^2+y^2+z^2}$ and θ is the angle between the position vector and the vertical axis.

Since the source is vertically directed, there is azimuthal symmetry. We choose the (x,z)-plane and the Cartesian solution is

$$
\begin{aligned}
G_x &= \sin\theta G_r + \cos\theta G_\theta, \\
G_z &= \cos\theta G_r - \sin\theta G_\theta.
\end{aligned}
\tag{57}
$$

The 3D viscoelastic particle velocities can then be expressed as

$$
v_i(r,\omega) = -\mathrm{i}\omega W(\omega) G_i(r,\omega), \quad i = x, z,
\tag{58}
$$

where $-\mathrm{i}\omega$ represents the time derivative in the frequency domain and W is the Fourier transform of the source time history (see equation (42)). A numerical inversion to the time domain by a discrete Fourier transform yields the desired time-domain solution.

Table 1. Poro-elastic properties

Saturation patches

Steam	$\rho_{f1} = 100$ kg/m^3 $K_{f1} = 0.1$ GPa $\eta_1 = 3 \times 10^{-5}$ Pa s

Permeability heterogeneities

Frame	$K_{m1} = 2$ GPa $\mu_{m1} = 1$ GPa $\phi_1 = 0.35$ $\kappa_1 = 1.5$ darcy

Background medium

Grain	$\rho_{s2} = 2650$ kg/m^3 $K_{s2} = 35$ GPa $\mu_{s2} = 32$ GPa
Frame	$K_{m2} = 7$ GPa $\mu_{m2} = 9$ GPa $\phi_2 = 0.18$ $\kappa_2 = 0.1$ darcy
water	$\rho_{f2} = 990$ kg/m^3 $K_{f2} = 2.25$ MPa $\eta_2 = 0.001$ Pa s

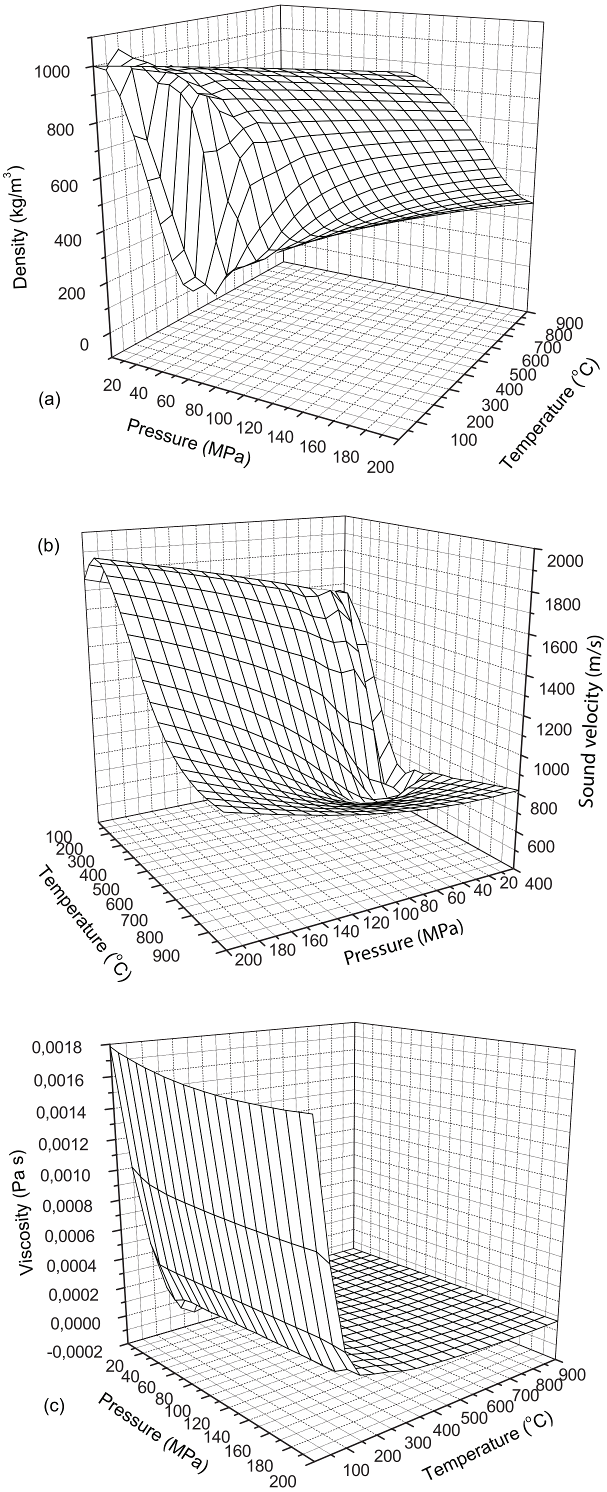

Fig. 1 Water density (a), sound velocity (b) and viscosity (c) for a wide range of pressures and temperatures (data taken from the NIST website).

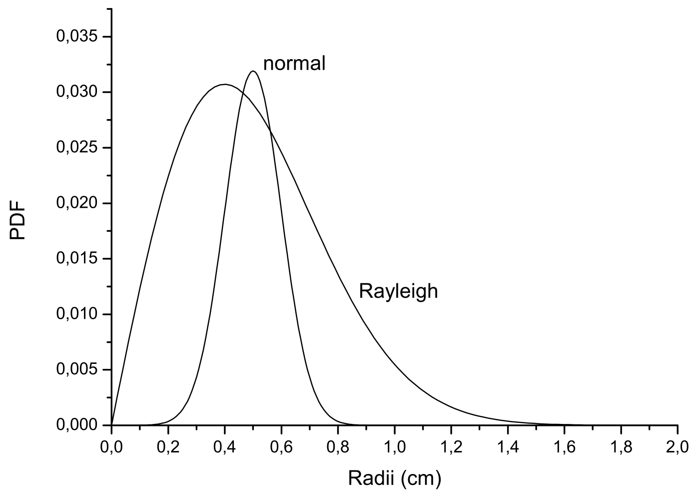

Fig. 2 Common PDFs to describe the distribution of the patch radii. The mean radius is $a_0 = 0.5$ cm.

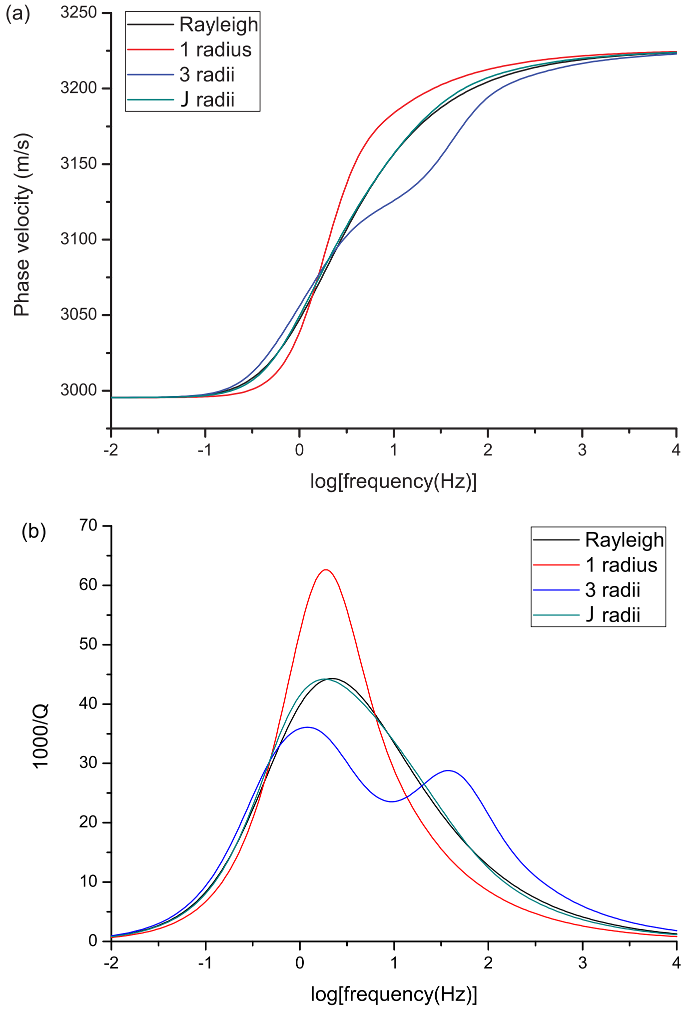

Fig. 3 P-wave phase velocity (38) (a) and dissipation factor (40) (b) versus frequency predicted by the generalized White model with different patch size distributions. 3 and J radii correspond to a uniform distribution.

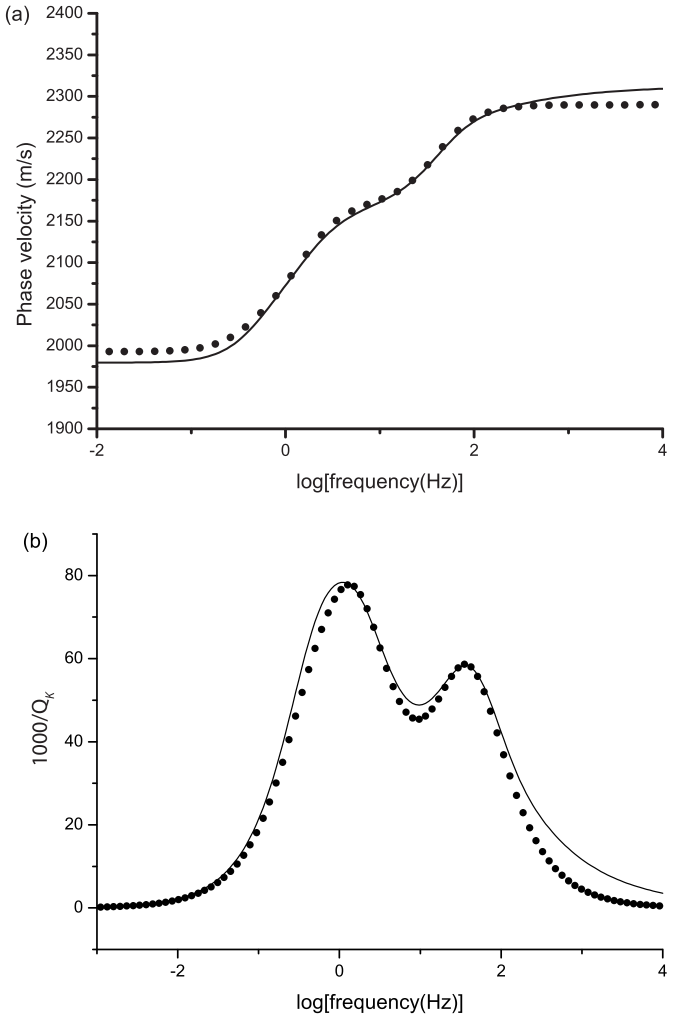

Fig. 4 Phase velocity (a) and dissipation factor (b) versus frequency associated with White bulk modulus K corresponding to the 3-radii distribution: (a) exact (solid line); (b) Zener approximation (dots).

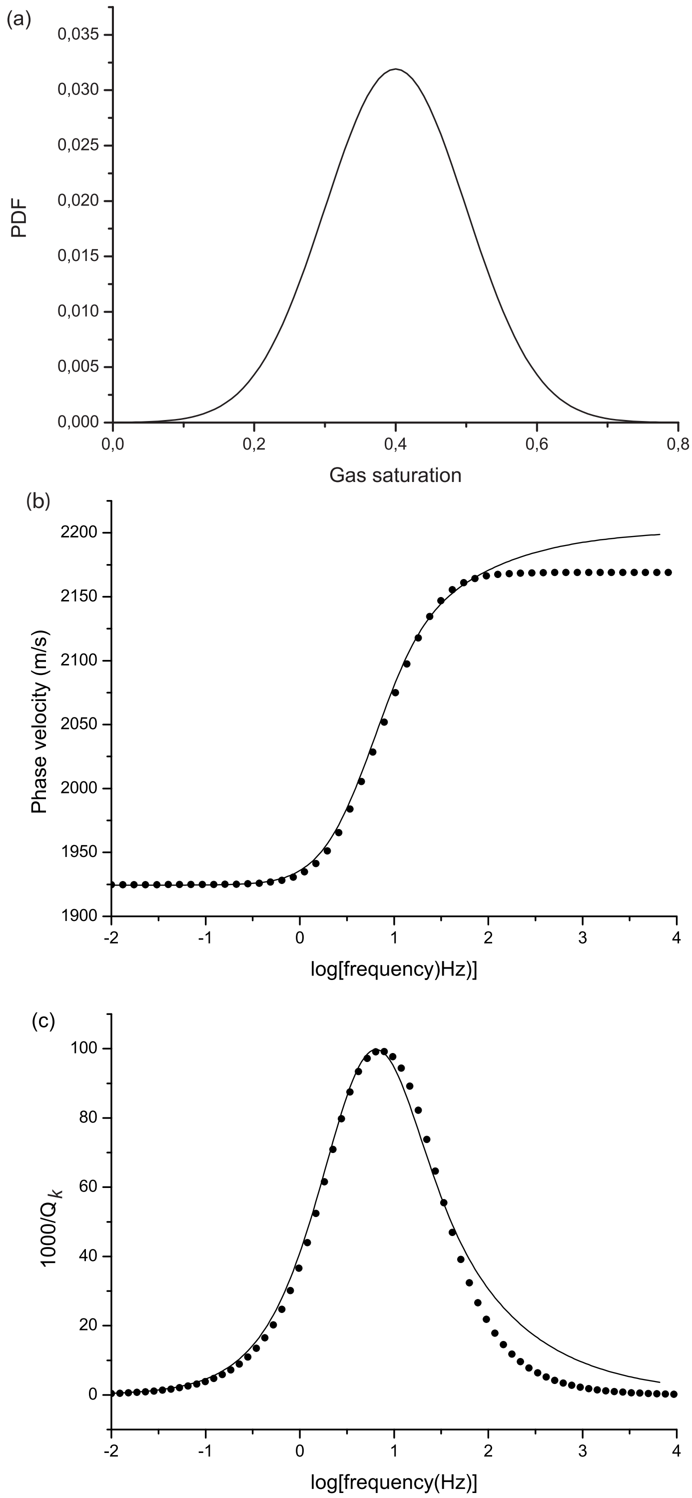

Fig. 5 Normal PDF (a), phase velocity (b) and dissipation factor (c) versus frequency associated with White bulk modulus corresponding to partial saturation: (a) exact (solid line); (b) 2-Zener approximation (dots).

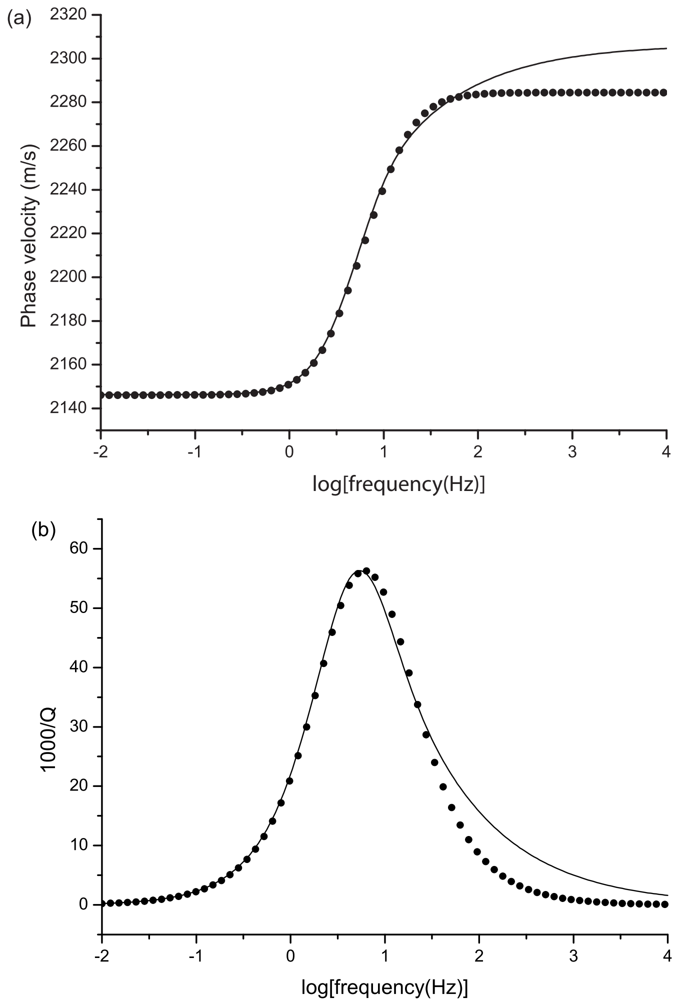

Fig. 6 Phase velocity (a) and dissipation factor (b) versus frequency associated with White P-wave modulus corresponding to permeability heterogeneities of different size determined by a normal PDF: (a) exact (solid line); (b) 2-Zener approximation (dots).

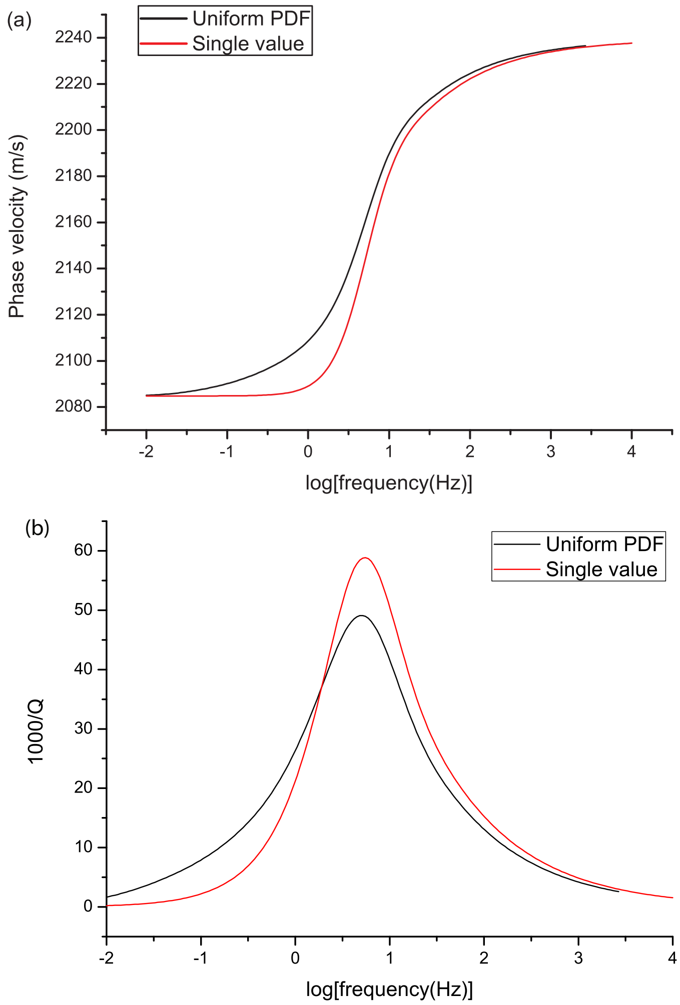

Fig. 7 Phase velocity (a) and dissipation factor (b) versus frequency associated with White P-wave modulus corresponding to permeability heterogeneities of size 0.5 m, whose values are determined by a uniform PDF. The red line corresponds to $\kappa_1 = 1$ darcy.

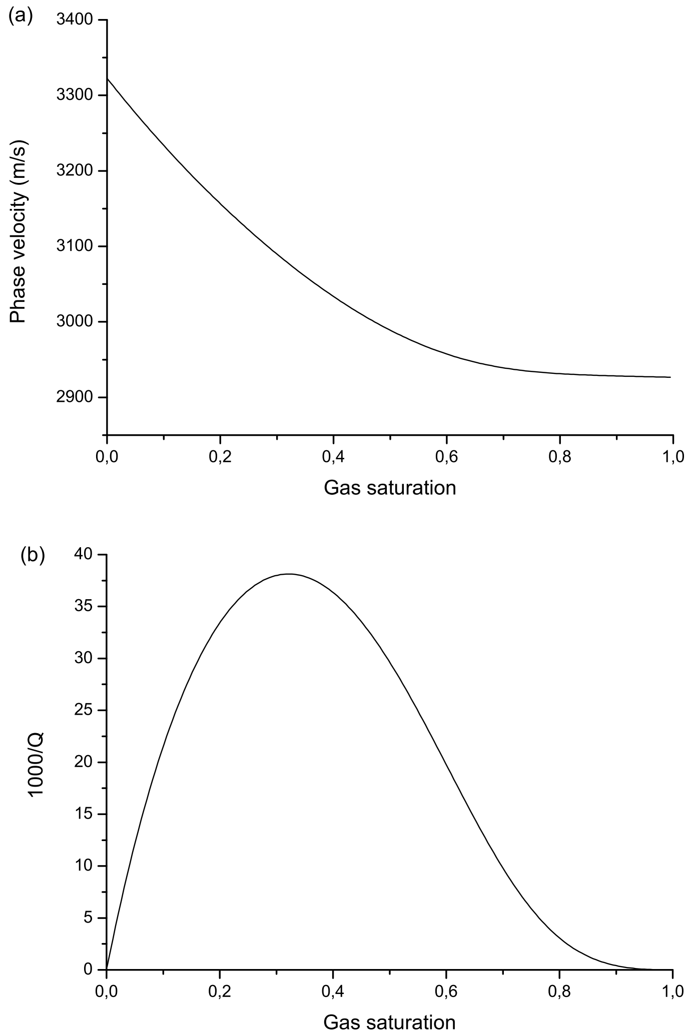

Fig. 8 P-wave phase velocity (38) (a) and dissipation factor (40) (b) as a function of steam saturation predicted by the generalized White model based on a Rayleigh PDF.

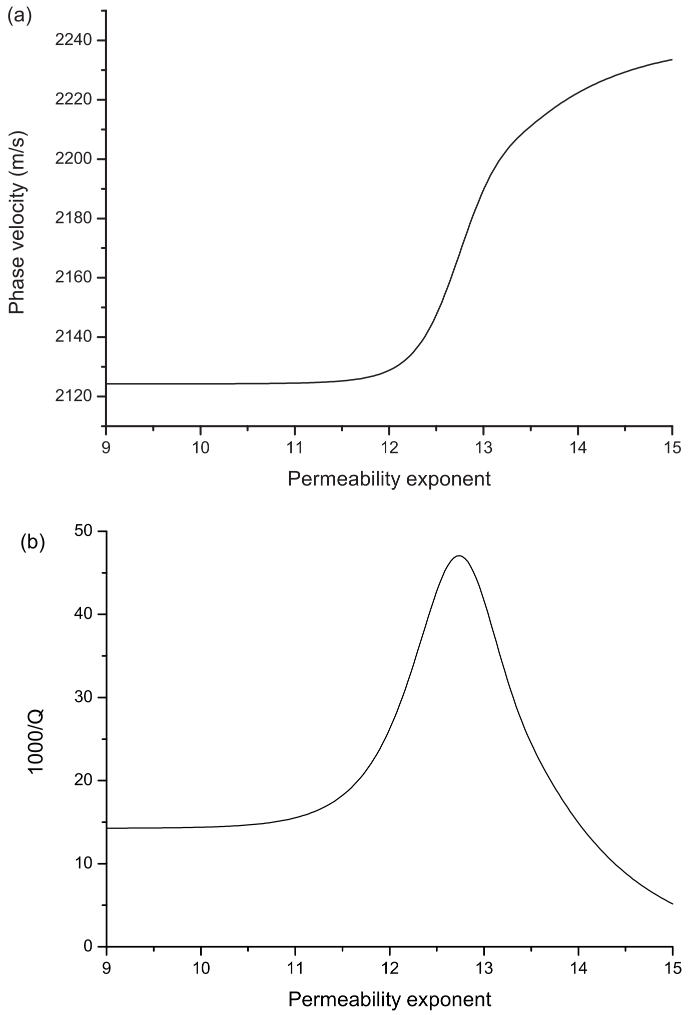

Fig. 9 Phase velocity (a) and dissipation factor (b) as a function of the exponent of the background permeability, p, ($\kappa_2 = 10^{-p}$ m^2) (p =12 refers to 1 darcy), associated with White P-wave modulus corresponding to permeability heterogeneities of size 0.5 m, whose values are determined by a uniform PDF.

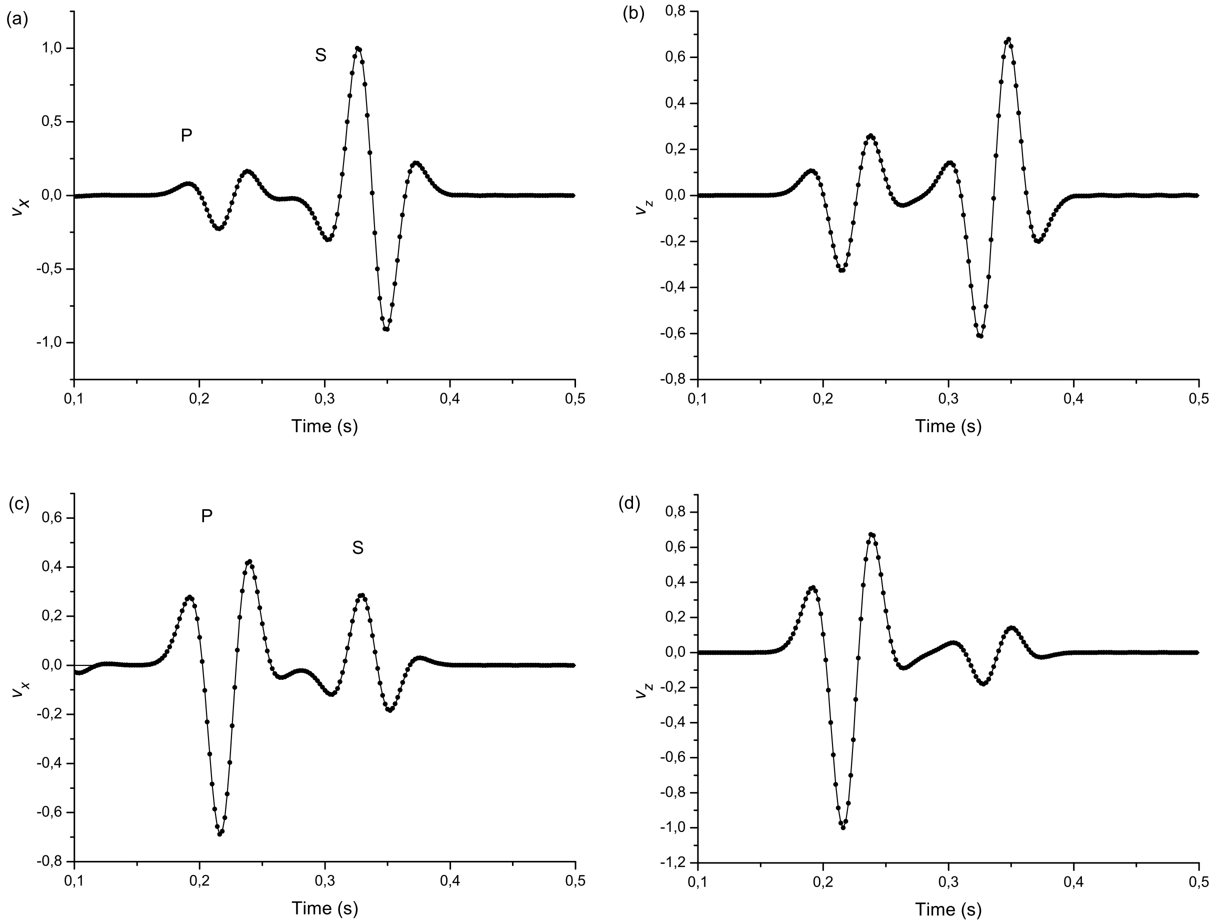

Fig. 10 Comparison between the analytical (solid line) and numerical (symbols) solutions for $\eta_B = 10^{20}$ Pa s (a and b) and $\eta_B = 2 \times 10^8$ Pa s (c and d). The horizontal (a and c) and vertical (b and d) particle velocities are shown. The fields are normalised. The amplitude of the S wave in (c) and (d) are much lower than in (a) and (b) due to attenuation arising from the plastic viscosity.

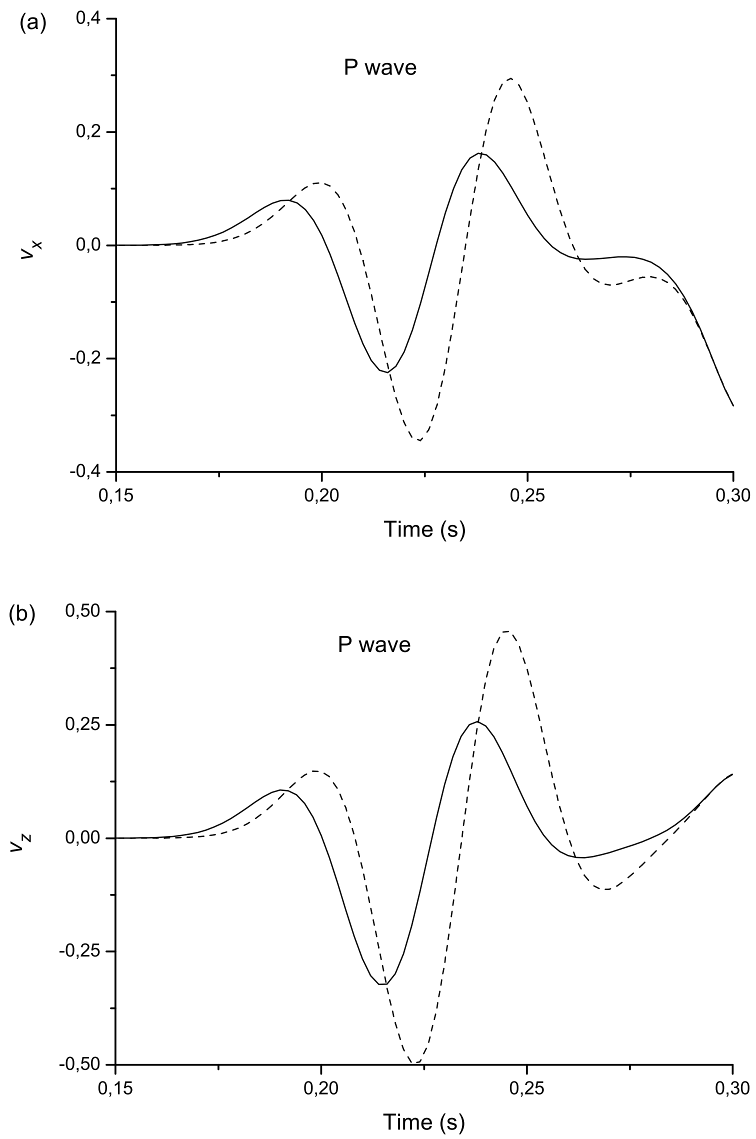

Fig. 11 Comparison between the solutions without (dashed line) and with (solid line) the mesoscopic loss for $\eta_B = 10^{20}$ Pa s. The horizontal (a) and vertical (b) particle velocities are shown. The fields are normalised.

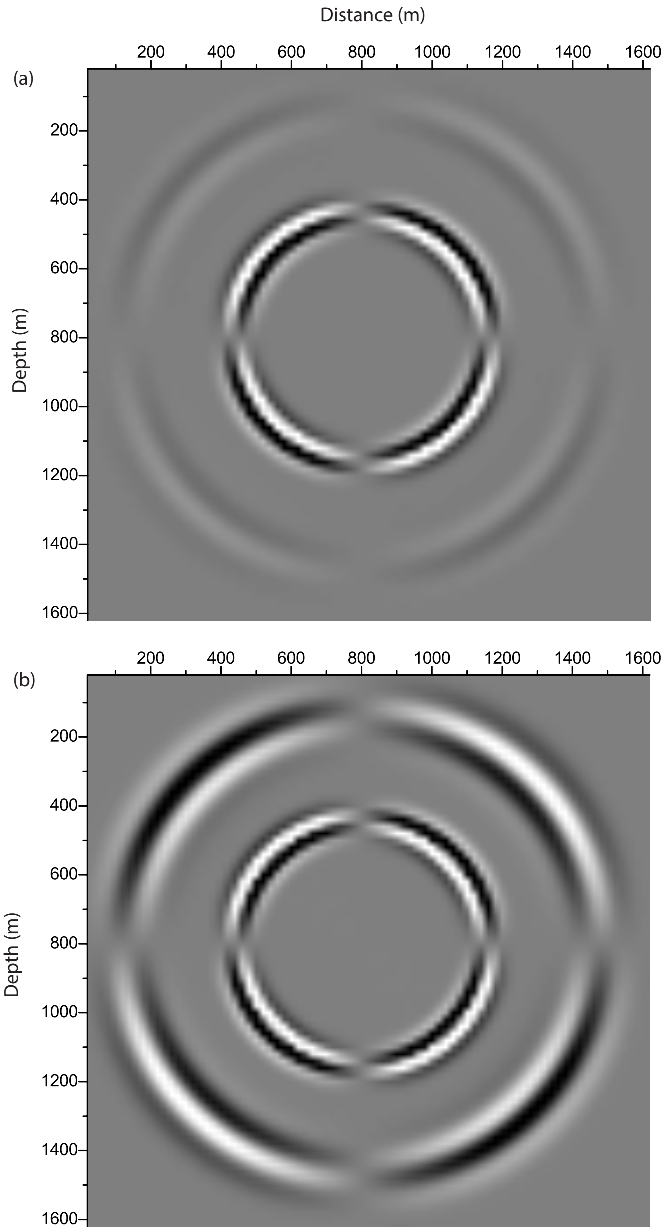

Fig. 12 Snapshots of the v_x component at 0.34 s. The field has been computed at the (x, z)-plane for $\eta_B = 10^{20}$ Pa s, with (a) and without (b) mesoscopic-loss.